A combined analysis of short-baseline neutrino experiments in the (3+1) and (3+2) sterile neutrino oscillation hypotheses

Michel Sorel,* Janet Conrad,† and Michael Shaevitz‡
Department of Physics, Columbia University, New York, NY 10027
(Dated: May 22, 2003)

We investigate adding two sterile neutrinos to resolve the apparent tension existing between short-baseline neutrino oscillation results and CPT-conserving, four-neutrino oscillation models. For both (3+1) and (3+2) models, the level of statistical compatibility between the combined data set from the null short-baseline experiments Bugey, CHOOZ, CCFR84, CDHS, and KARMEN, on one hand, and the LSND data set on the other hand, is computed. A combined analysis of all six short-baseline experiments, including LSND, is also performed, to obtain the favored regions in neutrino mass and mixing parameter space for both models. Finally, three statistical tests to compare the (3+1) and the (3+2) hypotheses are discussed. All tests show that (3+2) models fit the existing short-baseline data significantly better than (3+1) models. In particular, we estimate that the null sets and LSND are compatible at the 93% and 55% combined confidence level, for (3+1) and (3+2) models, respectively.

PACS numbers: 14.60.Pq, 14.60.St, 12.15.Ff

I. INTRODUCTION

There currently exist three experimental signatures for neutrino oscillations. The two signatures seen originally in solar and atmospheric neutrinos have been verified by several experiments, including experiments carried out with accelerator and nuclear reactor sources. The results on atmospheric neutrinos can be explained by ν_μ disappearance due to oscillations [1, 2, 3], while the results on solar neutrinos can be explained by ν_e oscillations [4, 5]. The third signature is $\bar{\nu}_e$ appearance in a $\bar{\nu}_\mu$ beam, as seen by the short-baseline, accelerator-based LSND experiment at Los Alamos [6]. This signature is strong from a statistical point of view, being a 3.8σ excess, but further confirmation by an independent experiment is necessary. The MiniBooNE experiment at Fermilab will be able to confirm or refute the LSND signature in the near future, with an experimental setup providing different systematics and higher statistics than LSND [7].

Taken at face value, the three experimental signatures point to three independent mass splittings. Only three neutrino masses do not appear to be able to explain all of the three signatures [8, 9] (see, however, [10]). One way to solve this puzzle is to introduce different mass spectra for the neutrino and antineutrino sector, thereby requiring CPT-violation, but no extra neutrino generations [11]. Another possibility is to add additional neutrinos with no standard weak couplings, often called "sterile neutrinos".

In this paper we assume CPT- and CP-invariance, and we explore the possibility of adding one or two neutrino generations beyond the three active flavors assumed by the Standard Model. We focus on extensions of the neutrino sector where the addition of fourth and fifth mass eigenstates are responsible for the high Δm^2 LSND oscillations, and the three lower mass states explain solar and atmospheric oscillations. When only one sterile neutrino is added, these models are labelled as (3+1). The flavor content of the four neutrino mass eigenstates for these models is schematically shown in Fig.1a. The (3+1) hierarchy in Fig.1a is as opposed to the (2+2) hierarchy, where the solar and atmospheric mass splittings are separated from each other by the LSND Δm^2. The (2+2) models require a different global analysis from the one discussed in this paper. The simplest (2+2) models appear to be only marginally consistent with neutrino oscillations data [8, 12], even though more general (2+2) mass and mixing scenarios might represent a viable solution to explain solar, atmospheric, and LSND oscillations [13].

The (3+1) models are motivated by the criterion of simplicity in physics, introducing the most minimal

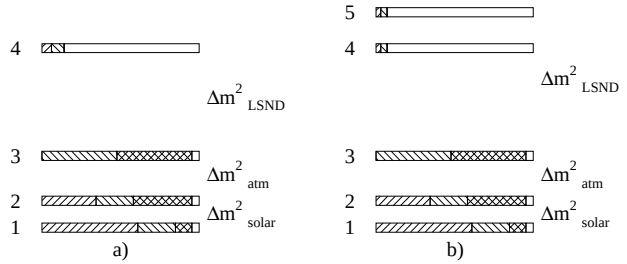

FIG. 1: Flavor content of neutrino mass eigenstates in (3+1) models (a), and (3+2) models (b). Neutrino masses increase from bottom to top. The ν_e fractions are inicated by right-leaning hatches, the ν_μ fractions by left-leaning hatches, the ν_τ fractions by crosshatches, the ν_s fractions by no hatches. The flavor contents shown are schematic only.

*Electronic address: sorel@fnal.gov
†Electronic address: conrad@fnal.gov
‡Electronic address: shaevitz@fnal.gov

extension to the Standard Model that explains the experimental evidence. However, theories invoking sterile neutrinos to explain the origin of neutrino masses do not necessarily require only one sterile neutrino. Indeed, many popular realizations of the see-saw mechanism introduce three right-handed neutrino fields [14, 15, 16]. From the phenomenological point of view, it is our opinion that two- and three-sterile neutrino models should also be considered and confronted with existing experimental results. In this paper, we consider the results from the short-baseline experiments Bugey [17], CCFR84 [18], CDHS [19], CHOOZ [20], KARMEN [21], and LSND [6], and examine how well (3+1) and (3+2) models agree with data. A schematic diagram for (3+2) models is shown in Fig.1b. We do not consider (3+3) models in this paper. From our initial studies, we believe that the phenomenology of a (3+3) model is similar to a (3+2) model.

The paper is organized as follows. In Section II, we specify the neutrino oscillations formalism used in this analysis to describe (3+1) and (3+2), short-baseline, oscillations. In Section III and IV, we present the results obtained for the (3+1) and (3+2) models, respectively. For both models, we first derive the level of compatibility between the null short-baseline (NSBL) experiments and LSND. Second, we perform a combined analysis of all six short-baseline experiments (including LSND) to derive the preferred regions in neutrino mass and mixing parameter space. In Section V, we discuss three statistical tests to compare the (3+1) and (3+2) hypotheses. In Section VI, we briefly mention other experimental constraints on (3+1) and (3+2) models. In Appendix A, we describe the physics and statistical assumptions used in the analysis to describe the short-baseline experiments.

II. NEUTRINO OSCILLATIONS FORMALISM

Under the assumptions of CP- and CPT-invariance, the probability for a neutrino, produced with flavor α and energy E, to be detected as a neutrino of flavor β after travelling a distance L, is [22]:

$$P(\nu_\alpha \to \nu_\beta) = \delta_{\alpha\beta} - 4\sum_{j>i}^{n}\sum_{i=1}^{n} U_{\alpha,j}U_{\beta,j}U_{\alpha,i}U_{\beta,i}\sin^2 x_{ji} \tag{1}$$

where $\alpha = e, \mu, \tau, s$, (s being the sterile flavor), U is the neutrino mixing matrix, $x_{ji} \equiv 1.27\Delta m^2_{ji}L/E$, $\Delta m^2_{ji} \equiv m^2_j - m^2_i$, and n is the number of neutrino generations. Neglecting CP-violating phases, there are in general $(n-1)$ independent mass splittings, and $n^2 - n - n(n-1)/2$ independent mixing matrix elements. The situation simplifies considerably by considering short-baseline (SBL) data only. In this case, it is a good approximation to assume $x_{21} = x_{32} = 0$, and only $(n-3)$ independent mass splittings are present. Moreover, given the set of SBL experiments considered, the number of mixing matrix elements probed is only $2(n-3)$, as we show now for the (3+1) and (3+2) cases.

For (3+1) models, n=4, and only one mass splitting $\Delta m^2 \equiv \Delta m^2_{41} \simeq \Delta m^2_{42} \simeq \Delta m^2_{43}$ appears in the oscillation formula: this is sometimes referred to as to the "quasi-two-neutrino approximation", or "one mass scale dominance" [23]. Using the unitarity properties of the mixing matrix, we can rewrite Eq.1 for (3+1) models in a more convenient way:

$$P(\nu_\alpha \to \nu_\beta) = \delta_{\alpha\beta} - 4U_{\alpha4}U_{\beta4}(\delta_{\alpha\beta} - U_{\alpha4}U_{\beta4})\sin^2 x_{41} \tag{2}$$

which depends on the mass splitting (Δm^2_{41}) and mixing parameters ($U_{\alpha4},\ U_{\beta4}$) of the fourth generation only. Since the two-neutrino approximation is satisfied in the (3+1) case, we can express Eq.2 in the usual forms:

$$P(\nu_\alpha \to \nu_\beta) = \sin^2 2\theta_{\alpha\beta}\sin^2 x_{41},\ \alpha \neq \beta \tag{3}$$

$$P(\nu_\alpha \to \nu_\alpha) = 1 - \sin^2 2\theta_{\alpha\alpha}\sin^2 x_{41} \tag{4}$$

where Eq.3 applies to an oscillation appearance measurement, Eq.4 to a disappearance measurement.

In this paper, we use the data from the Bugey, CCFR84, CDHS, CHOOZ, KARMEN, and LSND experiments. Bugey and CHOOZ data constrain $\bar{\nu}_e$ disappearance, CCFR84 and CDHS data constrain ν_μ disappearance, KARMEN and LSND data constrain $\bar{\nu}_\mu \to \bar{\nu}_e$ oscillations. Therefore, from Eqs.2,3, and 4, the experiments constrain the following combinations of (3+1) mixing parameters:

- Bugey, CHOOZ: $\sin^2 2\theta_{ee} \equiv 4U^2_{e4}(1 - U^2_{e4})$;
- CCFR84, CDHS: $\sin^2 2\theta_{\mu\mu} \equiv 4U^2_{\mu4}(1 - U^2_{\mu4})$;
- KARMEN, LSND: $\sin^2 2\theta_{\mu e} \equiv 4U^2_{e4}U^2_{\mu4}$.

In (3+1) models, the tension between the experimental results comes about because Bugey, CHOOZ, CCFR84, CDHS, and Karmen limit the two independent mixing matrix parameters U_{e4} and $U_{\mu4}$ to be small, whereas LSND demands nonzero values.

In (3+2) models, we introduce two sterile neutrinos. Using Eq.1 and the unitarity of the mixing matrix, the (3+2) neutrino oscillation formula can be written as:

$$P(\nu_\alpha \to \nu_\beta) = \delta_{\alpha\beta} - 4[(\delta_{\alpha\beta} - U_{\alpha4}U_{\beta4} - U_{\alpha5}U_{\beta5})(U_{\alpha4}U_{\beta4}\sin^2 x_{41} + U_{\alpha5}U_{\beta5}\sin^2 x_{51}) + U_{\alpha4}U_{\alpha5}U_{\beta4}U_{\beta5}\sin^2 x_{54}] \tag{5}$$

which in our case depends on two independent mass splittings ($\Delta m^2_{41}, \Delta m^2_{51}$) and four independent mixing matrix parameters ($U_{\alpha 4}$, $U_{\alpha 5}$, with $\alpha = e,\ \mu$). Eq.2 can be recovered from Eq.5 by requiring $U_{\alpha 5} = U_{\beta 5} = 0$. In (3+2) models, the quasi-two-neutrino-approximation is not valid, since there are three distinct Δm^2 values contributing in the oscillation formula: Δm^2_{41}, Δm^2_{51}, and Δm^2_{54}, and therefore three distinct oscillation amplitudes: $(\sin^2 2\theta_{\alpha\beta})_{41}$, $(\sin^2 2\theta_{\alpha\beta})_{51}$, and $(\sin^2 2\theta_{\alpha\beta})_{54}$.

III. RESULTS FOR (3+1) MODELS

This section, like the next one on (3+2) models, consists of two parts. First, we quantify the statistical compatibility between the NSBL and LSND results, following a method described in [24, 25], originally proposed to establish the compatibility between the LSND and KARMEN results. Second, we perform a combined analysis of the NSBL and LSND data sets, to obtain the favored regions in neutrino mass and mixing parameter space.

A. Statistical compatibility between NSBL and LSND

Many analyses of the NSBL experiments within (3+1) models have concluded that the allowed LSND region is largely excluded [26, 27, 28]. Here, we repeat this study with two purposes. First, we use this study to give context to our discussion of the basic model and techniques which will be expanded in later sections. Second, we demonstrate that our fit, which forms the basis of our new results for (3+2) models, reproduces the expected (3+1) exclusion region. For a discussion of the physics and statistical assumptions used to describe the short-baseline experiments used in the analysis, the reader should refer to Appendix A.

In this section, the NSBL and LSND data sets are analyzed separately, providing two independent allowed regions in $(\sin^2 2\theta_{\mu e}, \Delta m^2)$ space. The level of statistical compatibility between the two data sets can be determined by studying to what degree the two allowed regions overlap, as will be quantified later in this section.

In the analysis, we use a Monte Carlo method to generate random values for the mixing matrix elements U_{e4} and $U_{\mu 4}$, for any given value of neutrino mass splitting Δm^2. For each (3+1) model, we calculate the values for the χ^2 functions $\chi^2_{\rm NSBL}$ and $\chi^2_{\rm LSND}$, where $\chi^2_{\rm NSBL}$ is defined as:

$$\chi^2_{\rm NSBL} \equiv \chi^2_{\rm Bugey} + \chi^2_{\rm CHOOZ} + \chi^2_{\rm CCFR84} + \chi^2_{\rm CDHS} + \chi^2_{\rm KARMEN} \quad (6)$$

Throughout the paper, we make use of the Gaussian approximation in determining allowed regions in parameter space. In general, this means that the regions of quoted confidence level are the ones enclosed by contours of constant χ^2 values, whose differences with respect to the best-fit χ^2 value depend on the number of free parameters in the model [29]. In the text, we use the symbol δ to denote the values of the confidence levels derived in this way. As pointed out in [30], this approach should be considered approximate, as it may provide regions in parameter space of both higher and lower confidence than the one quoted. Regions of higher confidence than the quoted value may result in the presence of highly correlated parameters. Regions of lower confidence may result in the presence of fast oscillatory behavior of the oscillation probability formula, Eq.1. As we explain the procedures used in the analysis, we will comment on the effect that this approximation may have on our results.

For the analysis described in this section, the NSBL and LSND allowed regions are obtained using two different algorithms, reflecting the fact that the NSBL data set provides upper limits on oscillations, while the LSND data set points to non-null oscillations.

The NSBL allowed regions at various confidence levels $\delta_{\rm NSBL}$ are obtained via a raster scan algorithm [30]. Let $\chi^2_{\rm NSBL}$ be the χ^2 value for the particular model and $(\chi^2_{\rm NSBL})_{{\rm min},\Delta m^2}$ be the minimum χ^2 for the Δm^2 value considered. For example, our quoted 95% CL upper limit on $\sin^2 2\theta_{\mu e}$ is given by the maximum value for the product $4U^2_{e4}U^2_{\mu 4}$ chosen among the models which satisfy the inequality $\chi^2_{\rm NSBL} - (\chi^2_{\rm NSBL})_{{\rm min},\Delta m^2} < 5.99$. The value of 5.99 units of χ^2 is chosen because there are two free parameters U_{e4}, $U_{\mu 4}$ for (3+1) models with fixed Δm^2. We note that for the NSBL data set, the parameters U_{e4}, $U_{\mu 4}$ are mostly uncorrelated, only KARMEN probes the product of the two parameters.

The LSND allowed regions at various confidence levels $\delta_{\rm LSND}$ are obtained via a global scan algorithm [30]. For example, for $\delta_{\rm LSND} = 0.95$ we require $\chi^2_{\rm LSND} - (\chi^2_{\rm LSND})_{\rm min} < 5.99$, where $(\chi^2_{\rm LSND})_{\rm min}$ is now the global LSND χ^2 minimum value, considering all possible Δm^2 values. The LSND allowed region is computed for two free parameters as for the NSBL case, but the parameters are now Δm^2 and $U_{\mu 4}U_{e4}$, as opposed to $U_{\mu 4}$ and U_{e4}. Compared to the NSBL case, the number of free parameters is reduced by one because the LSND $\bar{\nu}_\mu \to \bar{\nu}_e$ search only probes the product $U_{\mu 4}U_{e4}$ and not the two mixing matrix elements individually, and it is increased by one because the allowed region is now obtained by scanning over all possible Δm^2 values.

Before discussing the results, we make two comments on this fit method. First, we require the neutrino mass splitting to be in the range $0.1\ eV^2 < \Delta m^2 < 100\ eV^2$. In Section VI, we briefly discuss why large mass splittings are not necessarily in contradiction with cosmological (and other) data. The values of the mixing parameters, U_{e4} and $U_{\mu 4}$, are randomly generated only within $U^2_{e4} + U^2_{\mu 4} < 0.5$, since large values for U_{e4} and $U_{\mu 4}$ are not allowed by solar and atmospheric neutrino data. Since the CDHS constraint on ν_μ disappearance vanishes for $\Delta m^2 \simeq 0.3\ eV^2$, as shown in Appendix A, the upper limit on ν_μ disappearance from atmospheric neutrino experiments above the atmospheric Δm^2 should

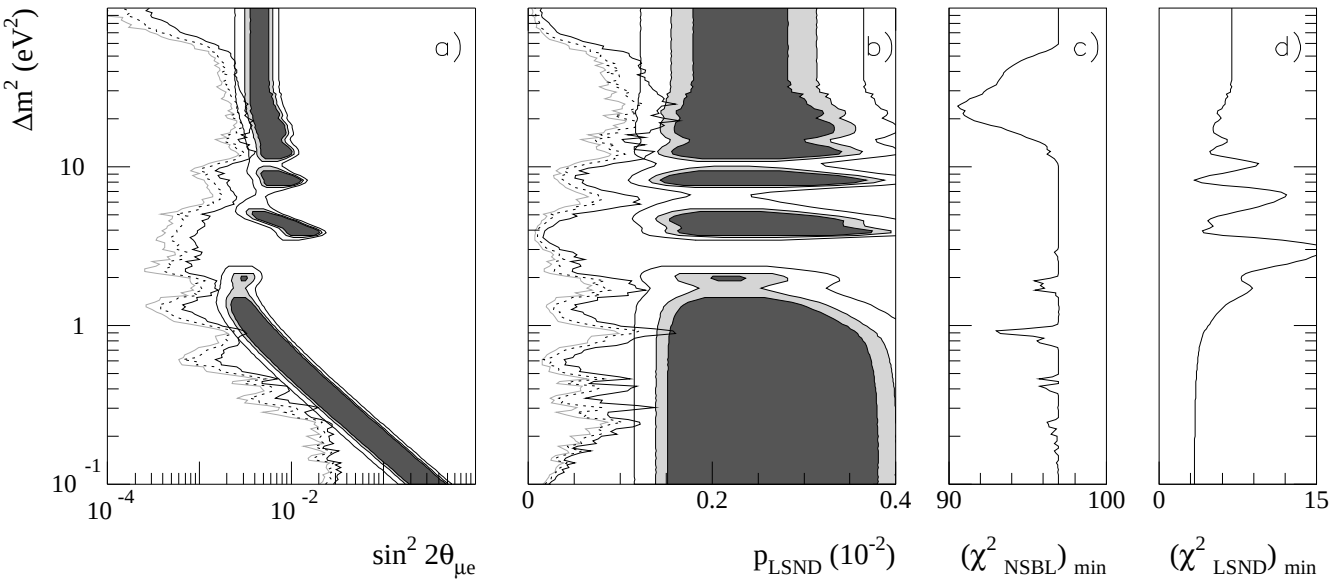

FIG. 2: Compatibility between the NSBL and LSND data sets in (3+1) models. Fig.2a shows the 90% (grey solid line), 95% (black dotted line), and 99% (black solid line) CL exclusion curves in $(\sin^2 2\theta_{\mu e}, \Delta m^2)$ space for (3+1) models, considering the null short-baseline (NSBL) experiments Bugey, CCFR84, CDHS, CHOOZ, and KARMEN. Fig.2a also shows the 90%, 95%, and 99% CL allowed regions by our analysis of LSND data. Fig.2b) is as Fig.2a, but in $(p_{\rm LSND}, \Delta m^2)$ space, where $p_{\rm LSND}$ is the LSND oscillation probability (see text for the definition). Fig.2c) and d) show the minimum χ^2 values as a function of Δm^2 for the NSBL and LSND data sets (113 and 3 dof, respectively).

be considered instead. In this paper, we do not reconstruct the likelihood for atmospheric data that would give the exclusion region for ν_μ disappearance in the range $\Delta m^2_{atm} \ll \Delta m^2 < 0.3\ eV^2$. However, the effect that the atmospheric constraints would have on the NSBL exclusion curve in Fig.2a is expected to be small. In Ref. [31], Bilenky *et al.* use the atmospheric up-down asymmetry to derive the upper limit $U^2_{\mu 4} < 0.55$ at 90% CL, which is satisfied by our initial requirement $U^2_{e4} + U^2_{\mu 4} < 0.5$.

Second, we comment on the procedure used to extract areas in parameter space of a given combined confidence δ from two independent experimental constraints, in our case obtained via the NSBL and LSND data sets, without assuming statistical compatibility *a priori*. The most straightforward way, described for example in [24, 25], is to assign a confidence level $\delta = \delta_{\rm NSBL}\delta_{\rm LSND}$ to the overlapping part (if any) between the two separate allowed regions in parameter space which are found with the constraint $\delta_{\rm NSBL} = \delta_{\rm LSND}$.

The regions allowed in parameter space by both the NSBL and LSND data sets are shown in Fig.2. The NSBL results alone allow the regions to the left of the solid grey, dotted black, and solid black lines in the Fig.2a, at a confidence level $\delta_{\rm NSBL} = 0.90,\ 0.95,\ 0.99$, respectively. In Fig.2a, the $\delta_{LSND} = 0.90,\ 0.95,\ 0.99$ CL allowed regions obtained by our analysis for LSND data are also shown, as dark grey shaded, light grey shaded, and white areas, respectively. We find no overlap between the two individual 95% CL allowed regions, corresponding to a combined confidence level $\delta = (0.95)^2 \simeq 0.90$; on the other hand, there is overlap between the two 99% CL regions, corresponding to the combined confidence $\delta \simeq 0.98$.

Fig.2b shows the same (3+1) allowed regions as Fig.2a but in the $(p_{\rm LSND}, \Delta m^2)$ plane, where $p_{\rm LSND}$ is defined as the $\nu_\mu \to \nu_e$ oscillation probability averaged over the LSND L/E distribution:

$$p_{LSND} \equiv \langle P(\nu_\alpha \to \nu_\beta) \rangle \qquad (7)$$

where $P(\nu_\alpha \to \nu_\beta)$ is given by the oscillation formula Eq.1 for $\alpha = e,\ \beta = \mu$, and is a function of all the mass and mixing parameters of the oscillation model under consideration. This has the obvious disadvantage of being a quantity dependent upon the specifics of a certain experiment, as opposed to a universal variable such as $4U^2_{\mu 4}U^2_{e4}$. However, $p_{\rm LSND}$ has the advantage of being unambiguously defined for any number of neutrino generations, and thus is useful in discussing (3+2) models later in this paper. As stated previously, the oscillation probability estimator $\sin^2 2\theta_{\mu e} = 4U^2_{\mu 4}U^2_{e4}$ cannot be used when more than one Δm^2 value affects the oscillation probability, as is the case for (3+2) models. A second advantage of using $p_{\rm LSND}$ instead of $\sin^2 2\theta_{\mu e}$ as the oscillation probability estimator, is that the allowed values for $p_{\rm LSND}$ inferred from the LSND result tend to be almost Δm^2-independent (see grey-shaded areas in Fig.2b), as expected for an almost pure counting experiment such as LSND. The oscillation probability reported by the LSND collaboration [6] is $p_{\rm LSND} = (0.264 \pm 0.067 \pm 0.045)\%$, and agrees well with our result of Fig.2b.

Fig.2c shows the values for $(\chi^2_{\rm NSBL})_{\rm min}$ as a function of Δm^2. The number of degrees of freedom is 113. A "mirror symmetry" between the NSBL exclusion curves in Figs.2a, 2b, and Fig.2c is apparent: the Δm^2 values for which the NSBL upper limits on $\sin^2 2\theta_{\mu e}$ and $p_{\rm LSND}$ are the least restrictive are also the Δm^2 values where the NSBL experiments marginally prefer the oscillation hypothesis to the no-oscillation one. As discussed in Appendix A, the dip in $(\chi^2_{\rm NSBL})_{\rm min}$ at $\Delta m^2 \simeq 0.9\ eV^2$ is due to Bugey data preferring $U_{e4} \neq 0$ values, while the minimum at $\Delta m^2 \sim 10 - 30\ eV^2$ is due to CDHS (mostly) and CCFR84 data, preferring $U_{\mu 4} \neq 0$ values. The χ^2 value for no oscillations, $(\chi^2_{\rm NSBL})_{\rm no\ osc}$, is the largest value in Fig.2c; this means that the choice of parameters $U_{e4} = U_{\mu 4} = 0$ provides the best-fit to NSBL data, for the Δm^2 values satisfying the condition $(\chi^2_{\rm NSBL})_{\rm min} = (\chi^2_{\rm NSBL})_{\rm no\ osc}$. Similarly, Fig.2d shows the values for $(\chi^2_{\rm LSND})_{\rm min}$ as a function of Δm^2, used to obtain the LSND allowed regions drawn in Figs.2a,2b.

We now present a slightly different approach to determine the statistical compatibility between the NSBL and LSND data sets in (3+1) models, which will prove useful in comparing the (3+1) and (3+2) hypotheses.

In Fig.3, we show the values for the χ^2 differences $\Delta\chi^2_{\rm NSBL}$, $\Delta\chi^2_{\rm LSND}$, as well as the corresponding confidence levels $\delta_{\rm NSBL}$, $\delta_{\rm LSND}$, as a function of the LSND oscillation probability. The curves are for the set of (3+1) models with the neutrino mass splitting Δm^2 fixed to the best-fit value obtained in a combined NSBL+LSND analysis (see Section III B), $\Delta m^2 = 23.8\ eV^2$, and mixing matrix elements $U_{\mu 4}$, U_{e4} treated as free parameters. The value for Δm^2 is chosen in this way because it represents to a good approximation the value for which one expects the best compatibility between the two data sets, as can also be seen in Fig.2b. In Fig.3a, we map the $(U_{e4}, U_{\mu 4})$ space into the $(p_{\rm LSND}, \chi^2_{\rm NSBL})$, $(p_{\rm LSND}, \chi^2_{\rm LSND})$ spaces. For any given value of $p_{\rm LSND}$, the minima for the $\chi^2_{\rm NSBL}$ and $\chi^2_{\rm LSND}$ functions are computed by standard minimization techniques [29] in the two (U_{e4}, $U_{\mu 4}$) and one ($U_{e4}U_{\mu 4}$) free parameters available, respectively. The process is repeated for several $p_{\rm LSND}$ values, and the collection of these minima for all values of $p_{\rm LSND}$ give the two curves in Fig.3a. The individual confidence levels $\delta_{\rm NSBL}$, $\delta_{\rm LSND}$, shown in Fig.3b, are obtained from $\Delta\chi^2_{\rm NSBL}$, $\Delta\chi^2_{\rm LSND}$ in the usual way.

From Fig.3b, we find overlapping allowed ranges in $p_{\rm LSND}$ for $1-\delta_{\rm NSBL} = 1-\delta_{\rm LSND} \simeq 3.6\%$. We conclude that, in (3+1) models, the LSND and NSBL data sets are compatible at a combined confidence of $\delta = (1 - 0.036)^2 \simeq 93\%$. In our opinion, this value does not support any conclusive statements against the statistical compatibility between NSBL and LSND data in (3+1) models, although it represents poor agreement between the two data sets. Future experimental constraints should be able to resolve this question.

B. Combined NSBL+LSND analysis

The second analysis we perform is a combined NSBL+LSND analysis, with the purpose of obtaining the (3+1) allowed regions in parameter space, in both $(\sin^2 2\theta_{\mu e}, \Delta m^2)$ and $(p_{\rm LSND}, \Delta m^2)$ space. A combined analysis of this sort assumes statistically compatible results. In Section III A, we have shown that the LSND and NSBL results are marginally compatible, for (3+1) models. In the following, we refer to the NSBL+LSND data set as the short-baseline (SBL) data set, and we construct the χ^2 function:

$$\chi^2_{\rm SBL} \equiv \chi^2_{\rm NSBL} + \chi^2_{\rm LSND} \tag{8}$$

where the two contributions $\chi^2_{\rm NSBL}$ and $\chi^2_{\rm LSND}$ are now simultaneously minimized with respect to the same set of oscillation parameters. Figs.4a and 4b show the 90%, 95%, and 99% CL allowed regions in $(\sin^2 2\theta_{\mu e}, \Delta m^2)$ and $(p_{\rm LSND}, \Delta m^2)$ space, respectively, from the combined (3+1) analysis of SBL data. In this combined analysis, we use the same Monte Carlo method described in Section III A. We define the allowed regions in parameter space by performing a global scan over the three free parameters Δm^2, U_{e4}, $U_{\mu 4}$, available in (3+1) models. For example, the 95% CL region is obtained by requiring $\chi^2_{\rm SBL} - (\chi^2_{\rm SBL})_{\rm min} < 7.82$, where $(\chi^2_{\rm SBL})_{\rm min}$ is the global minimum χ^2 value. Fig.4c shows the minimum $\chi^2_{\rm SBL}$ values obtained in the combined fit, as a function of Δm^2. Of course, the $\chi^2_{\rm SBL}$ values shown in Fig.4c for any given Δm^2 value are larger than the sum of the two contributions $\chi^2_{\rm NSBL}$, $\chi^2_{\rm LSND}$, shown in Figs.2c,d for the same Δm^2 value, since the latter were separately minimized with respect to the oscillation parameters.

We find two approximately equal minima of $\chi^2_{\rm SBL}$. The global minimum ($\chi^2_{\rm SBL}$=107.6, 118 dof) corresponds to the best-fit parameters $\Delta m^2 = 23.8\ eV^2$, $U_{e4} = 0.127$, $U_{\mu 4} = 0.219$. The second minimum ($\chi^2_{\rm SBL}$=109.5, 118 dof) corresponds to the parameters $\Delta m^2 = 0.91\ eV^2$, $U_{e4} = 0.135$, $U_{\mu 4} = 0.209$. Moreover, from Fig.4a,b, we find that the global minimum extends over a wide range of Δm^2 values, $10\ eV^2 < \Delta m^2 < 30\ eV^2$, while the second minimum for $\Delta m^2 = 0.91\ eV^2$ spans a much narrower range of Δm^2 values.

IV. RESULTS FOR (3+2) MODELS

A. Statistical compatibility between NSBL and LSND

Having introduced the relevant oscillation probability formula in Eq.5, and the statistical estimator $p_{\rm LSND}$ to compare the NSBL and LSND results in Section III A, we can now quantitatively address the statistical compatibility between the NSBL and LSND data sets under the (3+2) hypothesis.

Ideally, we would like to determine the NSBL upper

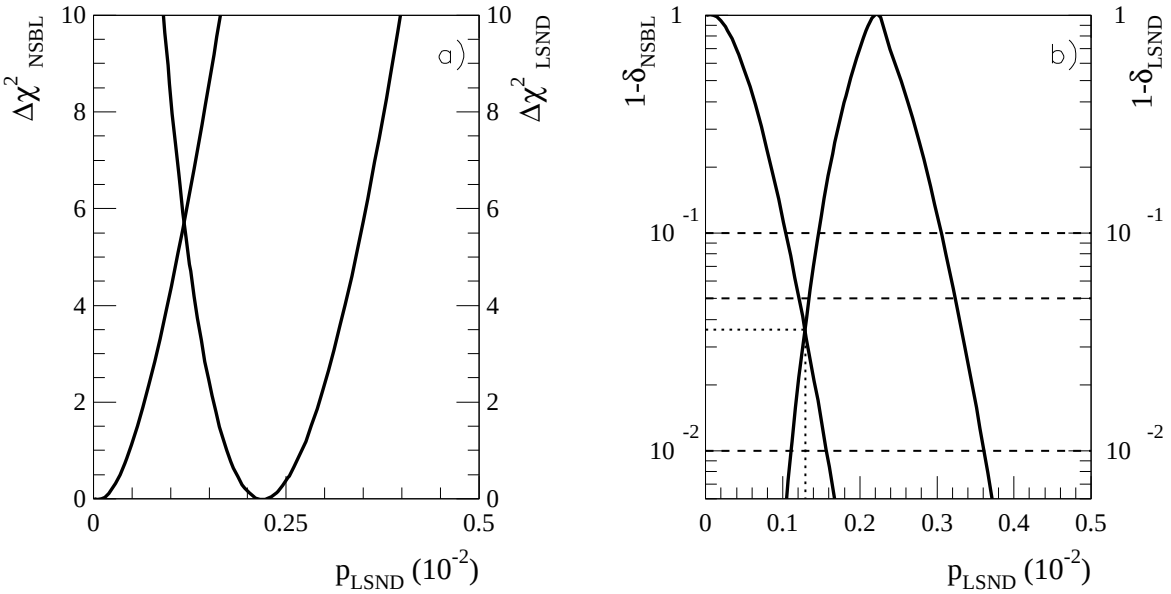

FIG. 3: a)χ^2 differences $\Delta\chi^2_{\rm NSBL}$, $\Delta\chi^2_{\rm LSND}$, and b) individual confidence levels $\delta_{\rm NSBL}$, $\delta_{\rm LSND}$, as a function of the LSND oscillation probability $p_{\rm LSND}$, for the NSBL and LSND data sets. The curves are for (3+1) models with the neutrino mass splitting Δm^2 fixed to the best-fit value $\Delta m^2 = 23.8\ eV^2$ from the combined NSBL+LSND analysis, and variable mixing matrix elements $U_{\mu 4}$, U_{e4}. The curves corresponding to the NSBL data set are the ones for $\Delta\chi^2_{\rm NSBL} = 0$ and $1 - \delta_{\rm NSBL} = 1$ at $p_{\rm LSND} = 0$. The dashed lines in Fig.3b refer to the 90%, 95%, 99% individual confidence levels, the dotted line gives the combined confidence level $\delta = \delta_{\rm NSBL}\delta_{\rm LSND}$ for which the NSBL and LSND data sets are compatible.

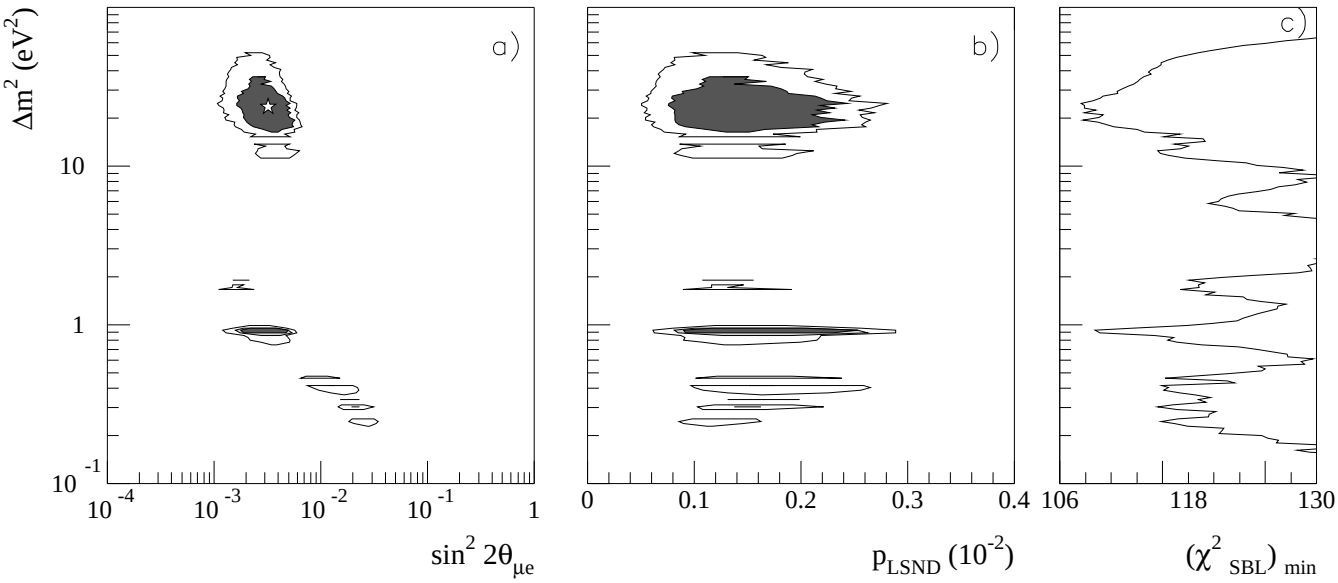

FIG. 4: Allowed regions in parameter space from a combined analysis of NSBL and LSND data, in (3+1) models, assuming statistical compatibility of the NSBL and LSND data sets. Fig.4a shows the 90%, 95%, and 99% CL allowed regions in $(\sin^2 2\theta_{\mu e}, \Delta m^2)$ space, together with the best-fit point, indicated by the star; b) shows the same allowed regions in $(p_{\rm LSND}, \Delta m^2)$ space; c) shows the minimum χ^2 value obtained in the combined analysis as a function of Δm^2. The number of degrees of freedom is 118.

limit for $p_{\rm LSND}$, for all possible combinations of the mass parameters Δm^2_{41}, Δm^2_{51}. This entails performing a scan equivalent to the one described in the (3+1) case as a function of Δm^2_{41}, shown in Fig.2. In practice, the CPU-time requirements to pursue this route were prohibitive.

An easier problem to tackle is to determine the statistical compatibility between the NSBL and LSND data sets only for the (3+2) models with mass splittings Δm^2_{41}, Δm^2_{51} fixed to their best-fit values, as obtained by the combined NSBL+LSND analysis that we present in Section IV B. In sections III A,III B, we have demonstrated that, at least for (3+1) models, this choice is a good approximation for the best possible statistical compatibility (see Figs.2, 4).

In Fig.5, we show the behavior of the χ^2 values $\Delta\chi^2_{\rm NSBL}$, $\Delta\chi^2_{\rm LSND}$, and of the confidence levels $\delta_{\rm NSBL}$, $\delta_{\rm LSND}$, as a function of $p_{\rm LSND}$, for the set of (3+2) models satisfying the requirements $\Delta m^2_{41} = 0.91\ eV^2$, $\Delta m^2_{51} = 21.5\ eV^2$. In analogy to Fig.3, we map the four-dimensional space $(U_{e4}, U_{\mu 4}, U_{e5}, U_{\mu 5})$ into the two-dimensional spaces $(p_{\rm LSND}, \chi^2_{\rm NSBL})$, $(p_{\rm LSND}, \chi^2_{\rm NSBL})$, and we plot the minimum χ^2 values obtained for any given value of $p_{\rm LSND}$. We now have four free parameters (U_{e4}, $U_{\mu 4}$, U_{e5}, $U_{\mu 5}$) in the $\chi^2_{\rm NSBL}$ minimization process, and two free parameters ($U_{e4}U_{\mu 4}$, $U_{e5}U_{\mu 5}$) for $\chi^2_{\rm LSND}$. The results presented in Fig.5a and the number of free parameters for the two data sets are used to extract the confidence levels shown in Fig.5b.

From Fig.5b, we find that, in (3+2) models, the NSBL and LSND data sets are compatible at the combined confidence level $\delta = \delta_{\rm NSBL}\delta_{\rm LSND} = 0.55$, and are, therefore, in good agreement with each other. Fig.5 should be compared to Fig.3, obtained for (3+1) models. A detailed comparison of the (3+1) and (3+2) hypotheses is presented in Section V.

B. Combined NSBL+LSND analysis

We now turn to a combined analysis of the NSBL and LSND data sets in (3+2) models. We have seen in Section IV A that the assumption of statistical compatibility between the two data sets is well justified. The purpose of this combined analysis is to obtain the allowed regions in the mass parameter space $(\Delta m^2_{41}, \Delta m^2_{51})$. Results will be shown for $\Delta m^2_{51} > \Delta m^2_{41}$; the case $\Delta m^2_{41} > \Delta m^2_{51}$ can be obtained by simply interchanging Δm^2_{41} with Δm^2_{51}. Again, because of the larger parameter space to be scanned in (3+2) models, we choose a slightly different and more robust numerical approach compared to the one used in the combined (3+1) analysis. We discretize the mass region of interest, $0.1\ eV^2 < \Delta m^2_{41}, \Delta m^2_{51} < 100\ eV^2$, into small cells in $(\Delta m^2_{41}, \Delta m^2_{51})$ space, and find the minimum value for $\chi^2_{\rm SBL}$ within the cell, using standard minimization techniques. The 95% CL allowed region is defined as the collection of cells for which $\chi^2_{\rm SBL} - (\chi^2_{\rm SBL})_{min} < 5.99$, where $\chi^2_{\rm SBL}$ is the minimum χ^2 value for the given cell, and $(\chi^2_{\rm SBL})_{min}$ is the absolute χ^2 minimum for all cells. In the minimization procedure, the mixing matrix elements U_{e4}, $U_{\mu 4}$, U_{e5}, $U_{\mu 5}$, are treated as free parameters.

Fig.6 shows the 90%, 95%, and 99% CL allowed regions in $(\Delta m^2_{41}, \Delta m^2_{51})$ space obtained in the combined (3+2) analysis. In light of the (3+1) analysis shown in previous sections, the result is not surprising, pointing to favored masses in the range $\Delta m^2_{41} \simeq 0.9\ eV^2$, $\Delta m^2_{51} \simeq 10 - 30\ eV^2$, at 90% CL. At 99% CL, the allowed region extends considerably, and many other $(\Delta m^2_{41}, \Delta m^2_{51})$ combinations appear. The best-fit point ($\chi^2_{\rm SBL}$=99.3, 118 dof) corresponds to the following set of parameters: $\Delta m^2_{41} = 0.91\ eV^2$, $U_{e4} = 0.117$, $U_{\mu 4} = 0.168$, $\Delta m^2_{51} = 21.5\ eV^2$, $U_{e5} = 0.065$, $U_{\mu 5} = 0.222$. We note here that the best-fit is not obtained for fourth and fifth mass eigenstates with degenerate masses, that is for $\Delta m^2_{41} \simeq \Delta m^2_{51}$.

V. COMPARING THE (3+1) AND (3+2) FITS TO SBL DATA

In this section, we discuss three statistical tests that can be used to quantify the better overall agreement of SBL data to a (3+2) hypothesis for neutrino oscillations, compared to a (3+1) one.

A. Test 1: NSBL upper limit on $p_{\rm LSND}$ at a given confidence level $\delta_{\rm NSBL}$

Test 1 uses only NSBL data to establish the (3+1) and (3+2) upper bounds on the LSND oscillation probability $p_{\rm LSND}$. From Figs.3,5, we obtain at a confidence level $\delta_{\rm NSBL} = 0.90$ (0.99):

(3+1): $p_{\rm LSND} < 0.104\%$ (0.158%)

(3+2): $p_{\rm LSND} < 0.197\%$ (0.280%)

Therefore, we find that (3+2) models can enhance the LSND probability $p_{\rm LSND}$ by quite a large factor, roughly 80%, compared to (3+1) models. The increase in $p_{\rm LSND}$ that we obtain is significantly larger than the 25% increase found in [26]. The value for the $\bar\nu_\mu \to \bar\nu_e$ oscillation probability measured by LSND [6] is $p_{\rm LSND} = (0.264 \pm 0.067 \pm 0.045)\%$, where the errors refer to the 1σ statistical and systematic errors, respectively.

B. Test 2: statistical compatibility between the NSBL and LSND data sets

Test 2 uses both the NSBL and LSND data sets, and treats them independently to find the combined confidence level $\delta = \delta_{\rm NSBL}\delta_{\rm LSND}$ for which the data sets are compatible, both in (3+1) and (3+2) models. The combined confidence levels can also be read from Figs.3,5:

(3+1): $\delta = 0.93$

(3+2): $\delta = 0.55$

Therefore, we find that in (3+1) models the two data sets are marginally compatible, and the agreement is significantly better in (3+2) models.

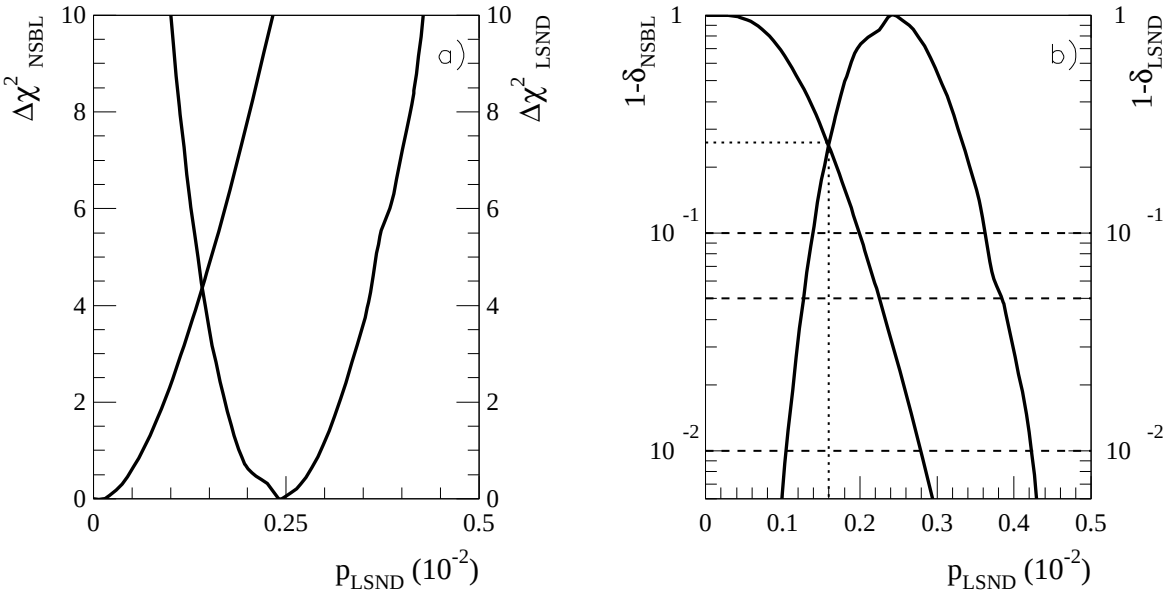

FIG. 5: a)χ^2 differences $\Delta\chi^2_{\rm NSBL}$, $\Delta\chi^2_{\rm LSND}$, and b) individual confidence levels $\delta_{\rm NSBL}$, $\delta_{\rm LSND}$, as a function of the LSND oscillation probability $p_{\rm LSND}$, for the NSBL and LSND data sets. The curves are for (3+2) models with the neutrino mass splittings Δm^2_{41}, Δm^2_{51}, fixed to the best-fit values $\Delta m^2_{41} = 0.91\ eV^2$, $\Delta m^2_{51} = 21.5\ eV^2$ from the combined NSBL+LSND analysis, and variable mixing matrix elements U_{e4}, $U_{\mu 4}$, U_{e5}, $U_{\mu 5}$. The curves corresponding to the NSBL data set are the ones for $\Delta\chi^2_{\rm NSBL} = 0$ and $1 - \delta_{\rm NSBL} = 1$ at $p_{\rm LSND} = 0$. The dashed lines in Fig.3b refer to the 90%, 95%, 99% individual confidence levels, the dotted line gives the combined confidence level $\delta = \delta_{\rm NSBL}\delta_{\rm LSND}$ for which the NSBL and LSND data sets are compatible.

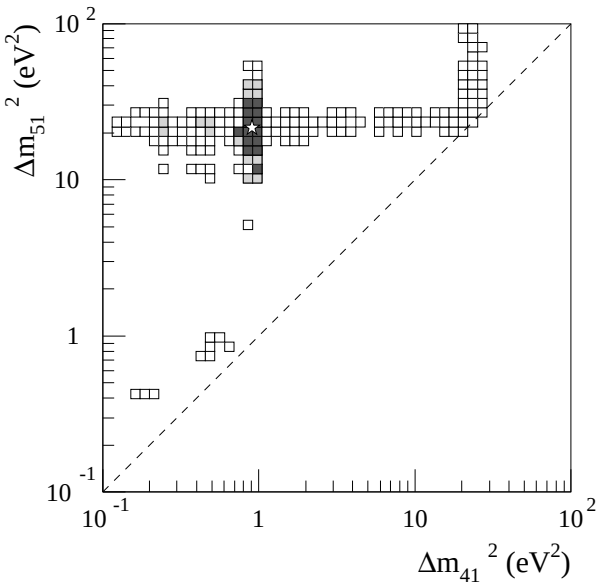

FIG. 6: Allowed ranges in $(\Delta m^2_{41}, \Delta m^2_{51})$ space for (3+2) models, for the combined NSBL+LSND analysis, assuming statistical compatibility between the NSBL and LSND data sets. The star indicates the best-fit point, the grey-shaded regions indicate the 90, 95, 99% CL allowed regions. Only the $\Delta m^2_{51} > \Delta m^2_{41}$ region is shown; the complementary region $\Delta m^2_{41} > \Delta m^2_{51}$ can be obtained by interchanging Δm^2_{41} with Δm^2_{51}.

C. Test 3: likelihood ratio test

Test 3 combines the NSBL and LSND data sets into a single, joint analysis. The likelihood ratio test [32] provides a standard way to assess whether two hypotheses can be distinguished in a statistically significant way. We define the maximum likelihood $\mathcal{L}_i$ from the minimum χ^2 values $(\chi^2_{\rm SBL})_{min,i}$ as $\mathcal{L}_i \equiv \exp(-(\chi^2_{\rm SBL})_{min,i}/2)$, where the index $i = 1, 2$ refers to the (3+1) and (3+2) hypotheses, respectively. We can then form the likelihood ratio $\lambda_{1,2} \equiv \mathcal{L}_1/\mathcal{L}_2$. If the (3+1) hypothesis were as adequate as the (3+2) hypothesis in describing SBL data, the quantity:

$$\chi^2_{1,2}(3) \equiv -2\ln\lambda_{1,2} = (\chi^2_{\rm SBL})_{\rm min,1} - (\chi^2_{\rm SBL})_{\rm min,2} \qquad (9)$$

should be distributed as a χ^2 distribution with three degrees of freedom, where the number of degrees of freedom is the difference in the number of mass and mixing parameters in the (3+2) and (3+1) hypotheses, 6-3=3.

In our combined fits, we obtain (see Sections III B,IV B):

(3+1): $(\chi^2_{\rm SBL})_{\rm min,1} = 107.6$, (118 dof)

(3+2): $(\chi^2_{\rm SBL})_{\rm min,2} = 99.3$, (115 dof)

and therefore $\chi^2_{1,2}(3) = 8.3$. This value is significantly larger than 3: the probability for a χ^2 distribution with three degrees of freedom to exceed the value 8.3 is only 4%. In other words, according to the likelihood ratio test,

the (3+1) hypothesis should be rejected compared to the (3+2) one at the 96% CL. Therefore, we conclude from test 3 also that (3+2) models fit SBL data significantly better than (3+1) models.

We can use the results of the likelihood ratio test between the (3+1) and (3+2) hypotheses to comment on the robustness of our conclusions, which rely on the Gaussian approximation to determine confidence level regions from constant χ^2 contours. The basic point is that the $(\chi^2_{\rm SBL})_{\rm min}$ value for the (3+2) model is lower than the $(\chi^2_{\rm SBL})_{\rm min}$ value for the (3+1) model by much more than would be expected for adding three random extra parameters. As we discussed, in the presence of highly correlated parameters, the quoted Gaussian confidence levels may correspond to levels of higher confidence, and therefore lead to overly optimistic conclusions concerning the statistical compatibility of the NSBL and LSND data sets considered here. In (3+2) models, the parameters U_{e4}, U_{e5}, as well as $U_{\mu 4}, U_{\mu 5}$, can potentially share a high degree of correlation, since those are constrained by the same experiments. For example, suppose that the degree of correlation between (3+2) parameters is such that setting confidence level regions for five "effective" parameters, as opposed to the actual six of (3+2) models, would provide a more accurate coverage. This would imply that (3+2) models differ from (3+1) ones by only two "effective" parameters, and not three. But in this case, the likelihood ratio test between the (3+1) and (3+2) hypotheses would acquire an even higher statistical significance in preferring (3+2) models to (3+1) ones (higher than the quoted 96% CL). Therefore, we believe that the overall conclusion that (3+2) models describe the short-baseline neutrino data better than (3+1) models, should hold true even when using an alternative statistical approach to the one adopted in this paper.

VI. ADDITIONAL CONSTRAINTS

The (3+1) and (3+2) models discussed in this work should be confronted with additional experimental constraints, other than the ones discussed in detail in the previous sections. Here, we limit ourselves to list, and comment on, some of these constraints, rather than address them in a quantitative way. Mostly, we will discuss the impact that such additional constraints may have on the best-fit (3+1) and (3+2) models found in Sections III and IV.

First, the set of short-baseline experiments considered in this analysis may be extended to add the results of $\nu_\mu \to \nu_e$ searches at $\Delta m^2 \simeq 10 - 100\ eV^2$. In this Δm^2 range, the NOMAD experiment provides the best sensitivity [33]. Preliminary results from the NOMAD Collaboration [33] on the $\nu_\mu \to \nu_e$ search give no evidence for oscillations, setting a 90% CL upper limit on the two-neutrino oscillation amplitude of $\sin^2 2\theta_{\mu e} = (1.2 - 2) \cdot 10^{-3}$, for $\Delta m^2 > 20\ eV^2$. Unfortunately, the amount of information published so far by the NOMAD Collaboration is not sufficient to include even a simplified characterization of the NOMAD constraints into our analysis. The NOMAD preliminary results would impact the findings of our combined (3+1) analysis discussed in Section III B, since the best-fit point shown in Fig.2a is obtained for $(\sin^2 2\theta_{\mu e} = 3 \cdot 10^{-3}, \Delta m^2 = 23.8\ eV^2)$, in contrast with the NOMAD bound. On the other hand, we obtain nearly equally good fits with lower Δm^2 (3+1) solutions, where the NOMAD bounds play a less significant role. Overall, the addition of NOMAD would be expected to push the best Δm^2 values slightly lower but not reduce the confidence levels significantly. Concerning (3+2) models, the combined analysis of Section IV B gives the following best-fit parameters: $\Delta m^2_{41} \simeq 0.91\ eV^2$, $U_{e4} \simeq 0.12$, $U_{\mu 4} \simeq 0.17$, $\Delta m^2_{51} \simeq 21.5\ eV^2$, $U_{e5} \simeq 0.07$, $U_{\mu 5} \simeq 0.22$, which would be interpreted in NOMAD as: $\Delta m^2 = \Delta m^2_{51} = 21.5\ eV^2$, $\sin^2 2\theta_{\mu e} = 4U^2_{e5}U^2_{\mu 5} \simeq 8 \cdot 10^{-4}$, which are compatible with the NOMAD limits listed above.

Second, nonzero mixing matrix elements U_{e4}, $U_{\mu 4}$, U_{e5}, $U_{\mu 5}$ may cause observable effects in atmospheric neutrino data, in the form of zenith angle-independent suppressions of the ν_μ and ν_e survival probabilities. Since our analysis of SBL data tends to give larger values for muon, rather than electron, flavor content in the fourth and fifth mass eigenstate, the effect should be larger on muon atmospheric neutrinos. For example, the (3+1) and (3+2) best-fit models from Sections III B,IV B would give an overall suppression of the ν_μ flux of 9% and 15%, respectively. The size of the effect of $\nu_\mu \to \nu_x$ oscillations at high Δm^2 is therefore comparable to the current accuracy with which the absolute normalization of the atmospheric neutrino flux is known [34], which is approximately 20%.

Third, models with large masses m_4, m_5, and nonzero mixing matrix elements U_{e4}, U_{e5}, should be confronted with the upper limits on the effective neutrino mass measured in tritium beta decay experiments, $m(\nu_e) = \sqrt{\sum_i^n |U_{ei}|^2 m_i^2}$, where n is the number of neutrino generations. The present constraint at 95% CL is $m(\nu_e) < 3\ eV$ [23]. In the case of a normal hierarchy for the neutrino masses, with $m_4, m_5 > m_1, m_2, m_3$, the best-fit (3+1) and (3+2) models obtained in our analysis predict $m(\nu_e) = 0.6\ eV$ and $m(\nu_e) = 0.3\ eV$, respectively, if we assume $m_1 = 0$. These values are in agreement with current tritium beta decay constraints. On the other hand, solutions based on a inverted hierarchy ($m_4, m_5 < m_1, m_2, m_3$) and with mass splittings $\Delta m^2 > 10\ eV^2$ would be severely constrained by the tritium beta decay results.

Fourth, introducing sterile neutrinos may affect a number of cosmological predictions, which have recently been precisely tested [35]. The standard cosmological model predicts that sterile neutrinos in the $\sim 1\ eV$ mass range with a significant mixing with active neutrinos would be present in the early Universe with the same abundance as the active neutrino species, in disagree-

ment with cosmological observations [36, 37]. On the other hand, several models have been proposed that would reconcile sterile neutrinos with cosmological observations, for example suppressing thermal abundances for sterile neutrinos (for a good review, see, *e.g.* Ref.[36] and references therein). In particular, active-sterile oscillations in the early Universe may provide a natural mechanism to suppress the relic abundances of sterile neutrinos [38], and scenarios invoking multiple sterile neutrinos are being investigated [37].

VII. CONCLUSIONS

We have performed a combined analysis of six short-baseline experiments (Bugey, CHOOZ, CCFR84, CDHS, KARMEN, LSND) for both the (3+1) and the (3+2) neutrino oscillation hypotheses, involving one and two sterile neutrinos at high Δm^2, respectively. The motivation for considering more than one sterile neutrino arises from the tension in trying to reconcile, in a CPT-conserving, four-neutrino picture, the LSND signal for oscillations with the null results obtained by the other short-baseline experiments. Multiple (*e.g.* three) sterile neutrinos can also be motivated on theoretical grounds.

We have described two types of analyses for both the (3+1) and (3+2) neutrino oscillation hypotheses. In the first analysis, we treat the LSND and the null short-baseline (NSBL) data sets separately, and we determine the statistical compatibility between the two. In the second analysis, we assume statistical compatibility and we combine the two data sets, to obtain the favored regions in neutrino mass and mixing parameter space.

The main results of the analysis are summarized in Section V, where we compare the adequacy of the (3+1) and (3+2) hypotheses in describing neutrino short-baseline data, by means of three statistical tests. First, we treat the LSND oscillation probability as a parameter that can be measured with NSBL data alone, and find that the NSBL upper limit on the LSND oscillation probability can be significantly relaxed by going from (3+1) to (3+2) models, by about 80%. Second, the combined confidence level for which the NSBL and LSND data sets are compatible is determined to be 93% and 55% in the analysis, for the (3+1) and (3+2) hypotheses, respectively. Third, a likelihood ratio test of the two hypotheses is discussed, and shows that (3+2) models fit the all of the short-baseline data significantly better than (3+1) models.

In conclusion, we find that (3+1) models are only marginally allowed when considering all of the six short-baseline results, including LSND, in agreement with previous analyses [26, 27, 28], and that (3+2) models can provide a much better description of the data. Only the simplest neutrino mass and mixing patterns have been fully characterized in the literature so far, and the analysis described in this paper may be viewed as a simple attempt to explore more generic scenarios, which appear both experimentally and theoretically plausible. Given the bright potential for precision measurements with neutrino oscillation experiments in the near future, a more general phenomenological approach may be needed.

Acknowledgments

We thank J. Bouchez, K. Eitel, E. A. Hawker, G. B. Mills, E. Nagy, and G. P. Zeller for kindly providing data used in this analysis. We thank K. N. Abazajian, G. Barenboim, S. J. Brice, K. Eitel, B. Kayser, W. C. Louis, J. Monroe, A. Y. Smirnov for valuable discussions and useful suggestions. This work was supported by NSF and by the Sloan Foundation.

APPENDIX A: PHYSICS AND STATISTICAL ASSUMPTIONS

In this section, we briefly describe the physics and statistical assumptions used to obtain the approximate characterizations of the short-baseline experiments used in the analysis. For the analysis of the Bugey, CDHS, and KARMEN data, we also refer to the excellent reference [28], which we followed closely.

The Bugey experiment [17] is sensitive to $\bar{\nu}_e$ disappearance by measuring the charged-current interaction of $\bar{\nu}_e$'s produced by two nuclear reactors at the Bugey nuclear power plant. Two liquid scintillator detectors, located at different positions, are used. The signature for an antineutrino interaction is a positron and a delayed light pulse produced by the subsequent neutron capture on ^6Li. Data are given for three baselines: 15, 40, and 95m between neutrino production and detection. We follow the "normalized energy spectra" analysis discussed in the Bugey paper [17]. The data are presented as ratios of observed to predicted (for no oscillations) positron energy spectra, between 1 and 6 MeV positron energy. We use 25,25, and 10 positron energy bins for the 15, 40, 95m baselines, respectively. In the χ^2 analysis, fits included not only the mass and mixing parameters, but also five large scale deformations of the positron spectrum due to systematic effects. The experimental positron energy resolution and the neutrino baseline smearing are taken into account, however the cross-section neutrino energy dependence within a positron energy bin are not (the energy bin widths are small).

The CHOOZ experiment [20], like Bugey, investigates $\bar{\nu}_e$ disappearance by observing interactions of $\bar{\nu}_e$'s produced by two nuclear reactors, $\simeq$ 1 km away from the CHOOZ detector. The signature for a neutrino interaction is a delayed coincidence between the prompt e^+ signal and the signal due to the neutron capture in the Gd-loaded scintillator. We follow "analysis A", as discussed in the CHOOZ paper [20]. Data are given as positron yields as a function of energy. In this analysis, seven positron energy bins, between 0.8 and 6.4 MeV, are considered, for which the CHOOZ observations, as

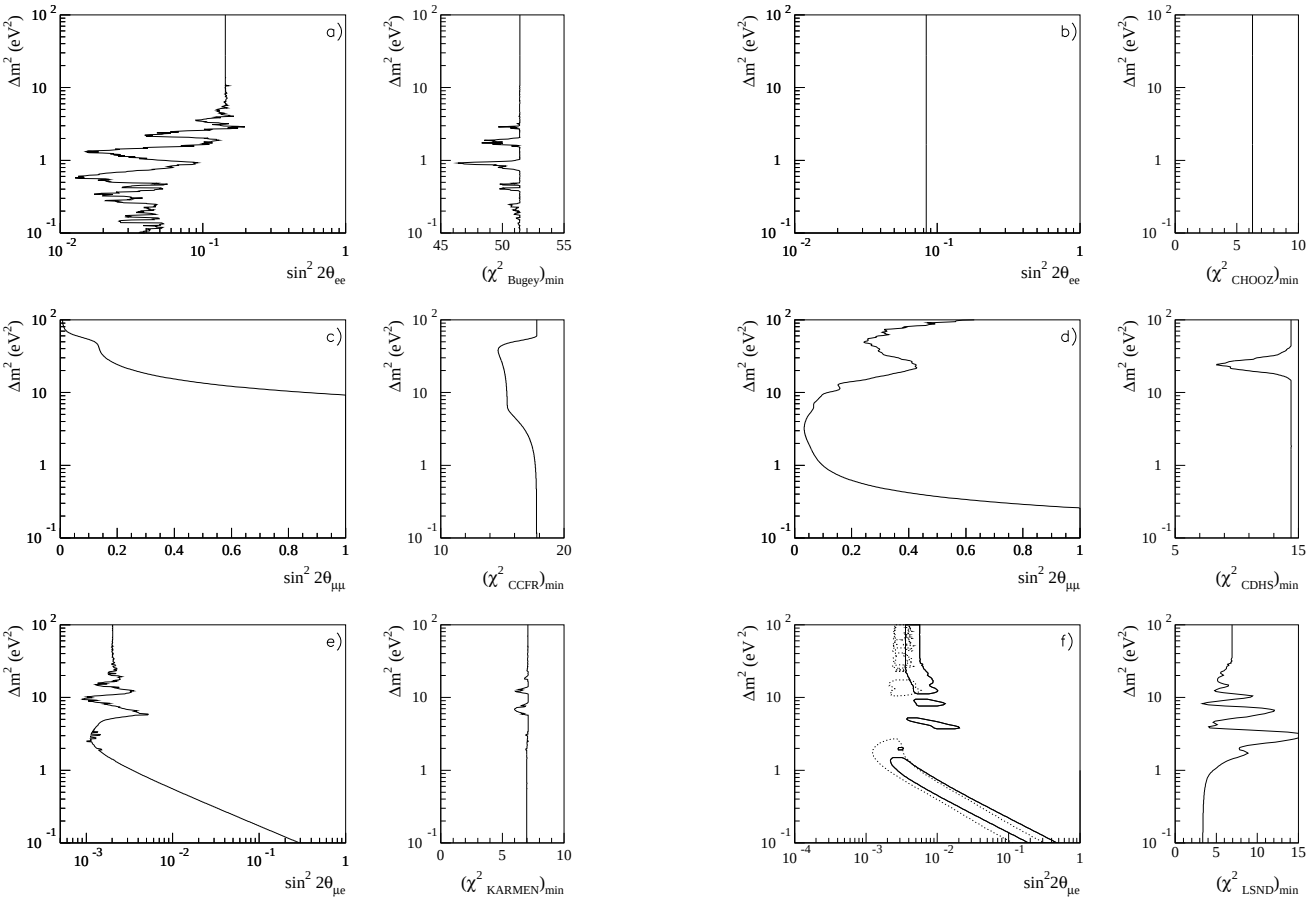

FIG. 7: 90% CL upper limits on oscillations derived in this analysis for the following NSBL experiments: a) Bugey, b) CHOOZ, c) CCFR84, d) CDHS, e) KARMEN. Fig.7f shows the LSND 90% CL allowed region obtained with the decay-at-rest analysis described in Appendix A (solid line), superimposed to the published LSND 90% CL allowed region (dashed line). Fig.7 shows also the $(\chi^2)_{\rm min}$ values as a function of Δm^2 obtained by all the experiments considered individually. The number of degrees of freedom is 58 in Bugey, 12 in CHOOZ, 16 in CCFR84, 13 in CDHS, 7 in KARMEN, 3 in LSND.

well as the predictions on the positron yields for the no-oscillation case from both reactors, are given in [20]. Because of the presence of two reactor sources, the χ^2 analysis comprises 14 positron yield bins for a given energy/baseline. We use the full covariance matrix to take into account the fact that the yields corresponding to the same energy bin are extracted for both reactors simultaneously, as is done in [20]. The analysis fits for the systematic uncertainty in the absolute normalization constant on the $\bar{\nu}_e$ yield from the reactors, in addition to the mass and mixing parameters. Since we are interested in the $\Delta m^2 > 0.1\ eV^2$ range only, where no energy shape distortions are expected, we neglect the systematic uncertainty on the energy-scale calibration, and the effect of the positron energy resolution.

The CCFR84 experiment [18] constrains ν_μ and $\bar{\nu}_\mu$ disappearance by measuring the charged-current interaction of muon neutrinos and antineutrinos, produced by a Fermilab secondary, sign selected, beam yielding $40 < E_\nu < 230$ GeV neutrinos from $\pi^\pm$ and $K^\pm$ decays in the 352m long decay pipe. We refer here to the 1984 CCFR experiment (hence the label CCFR84 throughout the text), which operated with two similar detectors located at different distances from the neutrino source, located at 715 and 1116m from the mid-point of the decay region. The two sampling calorimeter detectors consisted of steel plates and scintillation counters. Six secondary beam momentum settings were used, five for neutrino running, and one for antineutrino running. For each secondary beam momentum setting, the data are divided into three neutrino energy bins, for a total of eighteen energy bins, from Ref.[39]. Data are presented as double ratios: the far to near detector ratio of observed number of events, divided by the far to near ratio of events predicted for no oscillations. As in [18], only the mean neutrino energy for a given neutrino energy bin is used in the χ^2 analysis. The systematic and statistical uncertainties on the far to near ratio normalization are taken into account. The systematic uncertainty is assumed to be energy-independent and totally correlated between any two energy bins. The neutrino pathlength smearing, mostly due to the long decay region, is also

taken into account.

The CDHS experiment [19], like CCFR84, is sensitive to ν_μ disappearance via the charged-current interaction of ν_μ's, produced by a 19.2 GeV/c proton beam from the CERN Proton Synchrotron. Two detectors are located at 130 and 835 m from the target. The detectors are sampling calorimeters, with iron and scintillator modules interspersed, to measure the range of a muon produced in a neutrino interaction. Fifteen muon range bins are used. The data are presented as double ratios: the far to near detector ratio of the observed number of events, divided by the far to near ratio of the number of events predicted for no oscillations. Neutrino energy distributions are obtained for a given muon energy (or range) via the NUANCE [40] neutrino cross-section generator. As for CCFR84, the systematic uncertainty on the far to near ratio and the neutrino baseline smearing are taken into account.

The KARMEN experiment [21] investigates the $\bar{\nu}_\mu \to \bar{\nu}_e$ appearance channel, from $\bar{\nu}_\mu$'s produced in the π^+-μ^+-decay at rest (DAR) chain of the ISIS neutrino source. KARMEN measures the charged-current interaction $p(\bar{\nu}_e, e^+)n$, with a liquid scinitillator detector located at an average distance 17.7 m downstream of the neutrino source. The $\bar{\nu}_e$ signature is a spatially correlated delayed coincidence between a prompt positron and a delayed γ event from a (n, γ) neutron capture reaction. In this analysis, only the positron ("prompt") energy distribution after all cuts is taken into account, given in [21]. The data are binned into nine prompt energy bins, between 16 and 50 MeV (all bins are 4 MeV wide, except the highest energy one, ranging from 48 to 50 MeV). In predicting the prompt energy distribution for a set of mass and mixing oscillation parameters, the given Monte Carlo positron energy distribution, and the total number of events expected after all cuts for full mixing and $\Delta m^2 = 100\ eV^2$, are used [41]. Energy resolution and baseline smearing effects (due to finite detector size) are taken into account. Given the low statistics of the nine KARMEN prompt energy bins, we construct the χ^2 function by first defining the likelihood ratio [23]:

$$\lambda(\theta) = \frac{f(\mathbf{n}; \mu(\theta), \mathbf{b})}{f(\mathbf{n}; \mathbf{n}, \mathbf{b})} \tag{A1}$$

where θ denotes schematically all mass and mixing parameters, $\mathbf{n}$, $\mu(\theta)$ and $\mathbf{b}$ are the data, expected signal, and expected background vectors with nine elements, and $f(\mathbf{n}; \mu(\theta), \mathbf{b})$ are the probabilities for a Poisson process with known background:

$$f(\mathbf{n}; \mu(\theta), \mathbf{b}) = \sum_{i=1}^{9} \frac{(\mu_i + b_i)^{n_i} \exp(-(\mu_i + b_i))}{n_i!} \tag{A2}$$

We define $\chi^2_{\rm KARMEN}$ as:

$$\chi^2_{\rm KARMEN} \equiv -2 \ln \lambda(\theta) \tag{A3}$$

The LSND experiment at Los Alamos [6] is also sensitive to $\bar{\nu}_\mu \to \bar{\nu}_e$ appearance, with a similar neutrino source and neutrino detection signature as KARMEN, and better statistics. The LSND liquid scintillator detector is located at an average distance of 30m from the neutrino source. As for KARMEN, in this analysis we consider only the positron energy distribution arising from a $\bar{\nu}_e$ interaction in mineral oil, published as five energy bins between 20 and 60 MeV [6]. In other words, our analysis ignores the information arising from the higher-energy neutrinos from pions decaying in flight, which has a smaller (but non-negligible) sensitivity to oscillations compared to the decay at rest (DAR) sample considered here. In our simulation, we take into account the expected energy distribution from μ^+ decay at rest, the neutrino baseline distribution for the 8m long cylindrical detector, the neutrino energy dependence of the cross-section for the detection process $p(\bar{\nu}_e, e^+)n$ (including nuclear effects, simulated with the NUANCE [40] neutrino cross-section generator), and the experimental energy resolution. We use the published numbers for the background expectations, the number of $\bar{\nu}_e$ events for 100% $\bar{\nu}_\mu \to \bar{\nu}_e$ transmutation, and for the efficiency of the event selection criteria. We construct the LSND χ^2 function in the same way as we construct the KARMEN one, because of the low statistics of the data sample.

In Fig.7, we show the 90% CL upper limits on oscillations as a function of Δm^2 for the five NSBL experiments considered here, as well as the 90% CL allowed region for LSND. The $(\chi^2)_{\rm min}$ values as a function of Δm^2 for all of the experiments are also shown. All the solid curves shown are obtained from the simplified analysis described here, and compare well with the published results [6, 17, 18, 19, 20, 21].

The LSND region obtained in our analysis of DAR neutrinos is slightly shifted to the right compared to the final LSND area, shown in Fig.7f as a dashed line, reflecting the difference in the two data sets. More detailed LSND DAR analyses give results in rough agreement with our allowed region [12, 24].

The $(\chi^2)_{\rm min}$ values obtained for the Bugey and CDHS experiments as a function of Δm^2 give details that might seem surprising, at first. Slightly better fits to the data are obtained under a neutrino oscillations hypothesis, as opposed to the no oscillations one. Therefore, we add a final comment to explain the results of these fits.

The Bugey fit is driven by the data at the shortest baseline, 15 m, where the statistical errors on the observed positron spectrum from $\bar{\nu}_e$ interactions are the smallest. As explained in Ref.[17], systematic uncertainties are taken into account by allowing for linear deformations, as a function of positron energy, of the ratio of observed to predicted positron yields. The values of $(\chi^2_{\rm Bugey})_{\rm min}$ as a function of Δm^2 are explained by the fact that, for certain Δm^2 values, an oscillatory fit to the 15 m positron spectrum ratio describes the data marginally better than any straight line.

For CDHS, the $(\chi^2_{\rm CDHS})_{\rm min}$ curve in Fig.7d has a minimum at $\Delta m^2 \simeq 20 - 30\ eV^2$. This minimum is due to the fact that the far/near ν_μ rate ratio, corrected

for the baseline and detector mass differences between the two detectors (as well as other minor effects), is measured to be slightly greater than one [19]: $R_{\rm corr} = 1.044 \pm 0.023 \pm 0.025$. This marginal deviation from one causes the fit procedure to prefer more ν_μ disappearance by oscillations in the near than in the far detector. Given the average ν_μ energy (3.2 GeV) and pathlength (130 m) for neutrinos interacting in CDHS the near detector, this condition is satisfied in the $\Delta m^2 = 20 - 30\ eV^2$ range.

[1] Y. Fukuda *et al.* [Kamiokande Collaboration], Phys. Lett. B **335**, 237 (1994); R. Becker-Szendy *et al.*, Nucl. Phys. Proc. Suppl. **38**, 331 (1995); W. W. Allison *et al.* [Soudan-2 Collaboration], Phys. Lett. B **449**, 137 (1999). [arXiv:hep-ex/9901024].

[2] Y. Fukuda *et al.* [Super-Kamiokande Collaboration], Phys. Rev. Lett. **81**, 1562 (1998) [arXiv:hep-ex/9807003].

[3] M. Ambrosio *et al.* [MACRO Collaboration], Phys. Lett. B **517**, 59 (2001) [arXiv:hep-ex/0106049].

[4] B. T. Cleveland *et al.*, Astrophys. J. **496**, 505 (1998); P. Anselmann *et al.* [GALLEX Collaboration], Phys. Lett. B **285**, 376 (1992). D. N. Abdurashitov *et al.*, Phys. Lett. B **328**, 234 (1994).

[5] Q. R. Ahmad *et al.* [SNO Collaboration], Phys. Rev. Lett. **87**, 071301 (2001) [arXiv:nucl-ex/0106015]; Q. R. Ahmad *et al.* [SNO Collaboration], Phys. Rev. Lett. **89**, 011301 (2002) [arXiv:nucl-ex/0204008]; S. Fukuda *et al.* [Super-Kamiokande Collaboration], Phys. Lett. B **539**, 179 (2002) [arXiv:hep-ex/0205075].

[6] C. Athanassopoulos *et al.* [LSND Collaboration], Phys. Rev. Lett. **77**, 3082 (1996) [arXiv:nucl-ex/9605003]; C. Athanassopoulos *et al.* [LSND Collaboration], Phys. Rev. C **58**, 2489 (1998) [arXiv:nucl-ex/9706006]; A. Aguilar *et al.* [LSND Collaboration], Phys. Rev. D **64**, 112007 (2001) [arXiv:hep-ex/0104049].

[7] A. O. Bazarko [BooNe Collaboration], arXiv:hep-ex/9906003.

[8] M. Maltoni, T. Schwetz and J. W. Valle, Phys. Rev. D **65**, 093004 (2002) [arXiv:hep-ph/0112103].

[9] C. Giunti, M. C. Gonzalez-Garcia and C. Pena-Garay, Phys. Rev. D **62**, 013005 (2000) [arXiv:hep-ph/0001101].

[10] G. Barenboim and F. Scheck, Phys. Lett. B **440**, 332 (1998) [arXiv:hep-ph/9808327]; G. Barenboim, A. Dighe and S. Skadhauge, Phys. Rev. D **65**, 053001 (2002) [arXiv:hep-ph/0106002].

[11] H. Murayama and T. Yanagida, Phys. Lett. B **520**, 263 (2001) [arXiv:hep-ph/0010178]; G. Barenboim, L. Borissov, J. Lykken and A. Y. Smirnov, JHEP **0210**, 001 (2002) [arXiv:hep-ph/0108199]; G. Barenboim, L. Borissov and J. Lykken, arXiv:hep-ph/0212116.

[12] M. Maltoni, T. Schwetz, M. A. Tortola and J. W. Valle, Nucl. Phys. B **643**, 321 (2002) [arXiv:hep-ph/0207157].

[13] H. Pas, L. G. Song and T. J. Weiler, arXiv:hep-ph/0209373.

[14] P. Ramond, arXiv:hep-ph/9809459.

[15] R. N. Mohapatra and R. E. Marshak, Phys. Rev. Lett. **44**, 1316 (1980) [Erratum-ibid. **44**, 1643 (1980)].

[16] R. R. Volkas, Prog. Part. Nucl. Phys. **48**, 161 (2002) [arXiv:hep-ph/0111326].

[17] Y. Declais *et al.*, Nucl. Phys. B **434**, 503 (1995).

[18] I. E. Stockdale *et al.*, Phys. Rev. Lett. **52**, 1384 (1984).

[19] F. Dydak *et al.*, Phys. Lett. B **134**, 281 (1984).

[20] M. Apollonio *et al.*, arXiv:hep-ex/0301017.

[21] B. Armbruster *et al.* [KARMEN Collaboration], Phys. Rev. D **65**, 112001 (2002) [arXiv:hep-ex/0203021].

[22] B. Kayser, arXiv:hep-ph/0211134.

[23] K. Hagiwara *et al.* [Particle Data Group Collaboration], Phys. Rev. D **66**, 010001 (2002).

[24] E. D. Church, K. Eitel, G. B. Mills and M. Steidl, Phys. Rev. D **66**, 013001 (2002) [arXiv:hep-ex/0203023].

[25] K. Eitel, New J. Phys. **2**, 1 (2000) [arXiv:hep-ex/9909036].

[26] O. L. Peres and A. Y. Smirnov, Nucl. Phys. B **599**, 3 (2001) [arXiv:hep-ph/0011054].

[27] A. Strumia, Phys. Lett. B **539**, 91 (2002) [arXiv:hep-ph/0201134].

[28] W. Grimus and T. Schwetz, Eur. Phys. J. C **20**, 1 (2001) [arXiv:hep-ph/0102252].

[29] F. James and M. Roos, Comput. Phys. Commun. **10**, 343 (1975).

[30] G. J. Feldman and R. D. Cousins, Phys. Rev. D **57**, 3873 (1998) [arXiv:physics/9711021].

[31] S. M. Bilenky, C. Giunti, W. Grimus and T. Schwetz, Phys. Rev. D **60**, 073007 (1999) [arXiv:hep-ph/9903454].

[32] W. T. Eadie, D. Drijard, F. E. James, M. Roos, B. Sadoulet, "Statistical Methods in Experimental Physics" (North Holland, Amsterdam, 1971).

[33] D. Gibin, Nucl. Phys. Proc. Suppl. **66**, 366 (1998); V. Valuev [NOMAD Collaboration], *Prepared for International Europhysics Conference on High-Energy Physics (HEP 2001), Budapest, Hungary, 12-18 Jul 2001*

[34] M. Honda, T. Kajita, K. Kasahara and S. Midorikawa, Phys. Rev. D **52**, 4985 (1995) [arXiv:hep-ph/9503439]; Y. Liu, L. Derome and M. Buenerd, Phys. Rev. D **67**, 073022 (2003) [arXiv:astro-ph/0211632].

[35] D. N. Spergel *et al.*, arXiv:astro-ph/0302209; W. J. Percival *et al.*, arXiv:astro-ph/0105252. J. M. O'Meara, D. Tytler, D. Kirkman, N. Suzuki, J. X. Prochaska, D. Lubin and A. M. Wolfe, Astrophys. J. **552**, 718 (2001) [arXiv:astro-ph/0011179]; W. L. Freedman *et al.*, Astrophys. J. **553**, 47 (2001) [arXiv:astro-ph/0012376].

[36] K. N. Abazajian, Astropart. Phys. **19**, 303 (2003) [arXiv:astro-ph/0205238].

[37] P. Di Bari, arXiv:astro-ph/0302433; P. Di Bari, Phys. Rev. D **65**, 043509 (2002) [arXiv:hep-ph/0108182].

[38] R. Foot, M. J. Thomson and R. R. Volkas, Phys. Rev. D **53**, 5349 (1996) [arXiv:hep-ph/9509327].

[39] I. E. Stockdale, FERMILAB-THESIS-1984-08.

[40] D. Casper, Nucl. Phys. Proc. Suppl. **112**, 161 (2002) [arXiv:hep-ph/0208030].

[41] K. Eitel *et al.* [KARMEN collaboration], Nucl. Phys. Proc. Suppl. **77**, 212 (1999) [arXiv:hep-ex/9809007].